Chapter 2

Development of a Quantitative Full-Field, Three-Dimensional Imaging Technique

This chapter describes the development of a quantitative, full-field three-dimensional imaging technique for measuring deformations in solids including transparent soft materials. The method presented here employs a laser scanning confocal microscope to acquire three-dimensional volumetric images, while a digital volume correlation algorithm is used to determine the full field displacements. In particular, the DVC computes the displacement of fluorescent microparticles embedded in a transparent agarose polymer. What follows is a detailed presentation of the quantitative full field three-dimensional imaging technique development and its validation, including in-depth description of laser scanning confocal microscopy (LSCM) and digital volume correlation (DVC).

2.1 Laser Scanning Confocal Microscopy (LSCM)

This section presents an overview of laser scanning confocal microscopy and discusses how its resolution along the optical imaging axis can be improved by means of a computationally efficient deconvolution algorithm.

2.1.1 Overview of Laser Scanning Confocal Microscopy

Confocal microscopy has emerged as a powerful imaging technique due to its optical sectioning capability, which enables construction of three-dimensional images. In conventional wide-field microscopy, light is collected from the entire sample volume, including the focal plane as well as all other planes. In confocal microscopy light is generally collected from the focal plane only. This is achieved by using a pinhole in front of a photomultiplier tube (PMT) detector that blocks the incoming light from all other planes. As illustrated in Fig. 2.1, the solid line represents light reflected or emitted from the focal plane, while the dashed lines represent light from the out-of-focus planes.

The overall contrast and resolution of the image is significantly increased as compared to conventional wide-field microscopy where the image is blurred by out-of-plane light. As a consequence, the inherent optical sectioning of the specimen in confocal microscopy allows the assembly of three-dimensional image volumes by stacking together individually acquired planar slices. In an LSCM system, a laser with a single-diffraction limited spot size is used to sequentially scan a selected focal plane. Thus, the image is not formed using a CCD camera as in conventional microscopy, but rather the image is a result of the lights interaction with successive areas of the specimen, i.e., the image is recorded pixel by pixel, analogous to a scanning electron microscope (SEM). The resulting image is generally superior in resolution to images recorded by conventional optical microscopy. The spatial resolution of a confocal microscope is determined by the three-dimensional point spread function (PSF), which is an intensity distribution near the focal point corresponding to a volume image of a point light source under a diffraction-limited imaging system. Thus, the obtained confocal image is the convolution of actual intensity distributions using the point spread function as

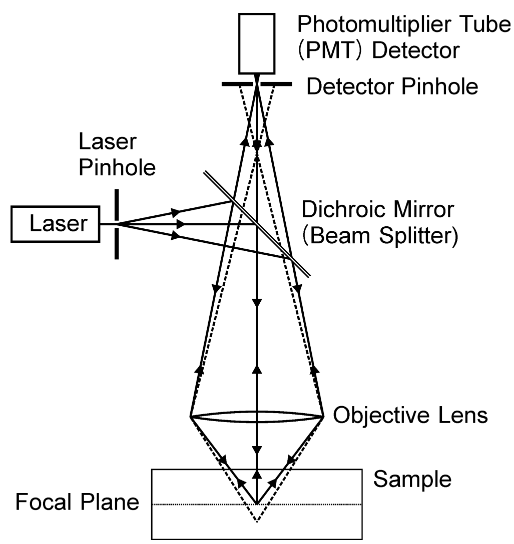

Figure 2.1: Illustration of the confocal imaging principle (solid lines = in-focus light; dashed lines = out-of-focus light)

a kernel or an optical impulse response function. A given point spread function will depend on each imaging situation but is typically a function of the imaging wavelength, λ, refractive index surrounding the lens, n, the numerical aperture of the lens, NA, and the image magnification. The numerical aperture of a lens can be expressed as $NA = nsin\theta$, where θ is the half angle of the light cone collected by the microscope lens. Following the derivations given by Stevens *et al.* [47], a representive expression for the intensity distribution of the point spread function along the lateral and optical imaging axis (u, v) gives

$$h^2[u,v] = |\int_0^1 J_0[v\rho]exp(iu\rho^2/2)\rho d\rho|^2, \tag{2.1}$$

where ρ is the radial distance from the optical axis and J_0 is the Bessel function of order zero. The optical coordinates u and v are related to the spatial coordinates r and z by

$$v = \frac{2\pi}{\lambda}(NA)r, \quad u = \frac{2\pi}{\lambda}(NA)^2 z/n, \tag{2.2}$$

where r is the radial distance from the optical axis, and z is the distance from the focal plane. Figure 2.2 shows a typical line intensity plot of the above point spread function expression both along the lateral and optical imaging axis. The lateral intensity profile of the point spread function in the focal plane, i.e., $h^2[0, v]$, gives the known line profile of the Airy disk[1]. Using Eqs. 2.2, estimates on the typical lateral and axial resolutions can be formulated by using the generally adopted Rayleigh criterion. This criterion states that the ultimate lateral resolution of the optical system is determined by the first zero of the Airy pattern or J_0.

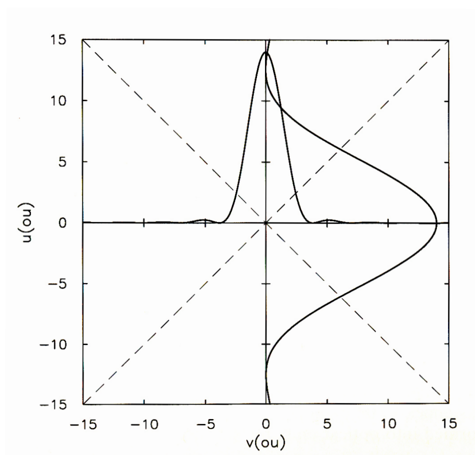

Figure 2.2: Profiles of the PSF for $u = 0$ (lateral), and $v = 0$ (vertical) from Stevens *et al.* [47]. The units of u and v are arbitrary optical units (ou). The peak widths determine the resolution.

[1]The interference pattern created from light diffracting through a circular aperture is known as the Airy disk

Following the same criterion in determining the axial direction, both lateral and axial resolution limits can be estimated as

$$Resolution_{lateral} = 0.61\frac{\lambda}{NA}, \tag{2.3}$$

and

$$Resolution_{axial} = 1.4\frac{n\lambda}{NA^2}. \tag{2.4}$$

This result is shown graphically in Fig. 2.2 by the width of both lateral and axial intensity peaks. Further details describing the confocal principle, including a more rigorously mathematical treatment of confocal imaging and the current applications of confocal microscopy, are well documented and can be found elsewhere [11, 43, 47, 19] . The next section will describe a method to improve the axial resolution of LSCM by accounting for the effects of the point spread function.

2.1.2 Improving Axial Resolution through Deconvolution

Figure 2.2 illustrates the differences in the lateral and axial resolutions during confocal imaging. As can be seen, the axial resolution of confocal imaging is typically three to ten times worse than the lateral resolution depending on the refractive index of the medium and the numerical aperture of the objective lens. In Fig. 2.3, an isosurface[2] plot of a typical confocal subvolume image (64 x 64 x 64 voxels) of a transparent agarose gel with randomly dispersed fluorescent spherical particles of two voxels in diameter is shown. A voxel is defined as a pixel in three-dimensional space, which in the present case is equal to 0.45 μm. The spherical fluorescent particles appear as axially elongated ellipsoids. The blurring in the axial direction causes increased uncertainties in the digital volume correlation measurements of the axial direction components. The consequence of such blurring is particularly critical to the performance of the large deformation digital volume correlation algorithm that uses the Fourier power spectrums. In this study, the noise-resistant Lucy-Richardson deconvolution algorithm [30] was used to deconvolve the raw confocal images using the following point

[2] An isosurface is a surface consisting of points of constant value

spread *sinc* function (PSF),

$$PSF = \frac{sin(x_3)}{x_3}, \tag{2.5}$$

in the axial direction prior to the stretch correlation. The appropriateness of using a *sinc* function in approximating the three-dimensional point spread function can be seen in Fig. 2.2, and from Eq. 2.1, where $h^2[u, 0]$ describes a typical *sinc* profile. Figure 2.4 shows the subvolume from Fig. 2.3 after deconvolution of the raw image.

There are two additional confocal-imaging artifacts caused by the refractive index mismatch in the optical path. First, spherical aberration due to the refractive index mismatch causes asymmetric distortions of the three-dimensional point spread function as a function of the penetration depth. Such a distorted and depth-dependent point spread function makes the deconvolution of the confocal images difficult and causes significant error in the digital volume correlation. Effects of such spherical aberration in confocal imaging have been extensively studied in the past [51, 44]. In practice, the spherical aberrations can be minimized by adjusting the correction collar commonly found in commercial microscope objectives. In order to minimize the distortion of the point spread function within the field of view, the correction collar needs to be adjusted appropriately prior to each test. The second form of confocal imaging artifact due to the refractive index mismatch is caused by the fact that the focal point does not follow the axial motion of the scanning stage [52, 15]. This causes an over- or under-estimation of the depths depending on the ratio of the refractive indeces. This apparent discrepancy between the axial and the lateral scanning resolutions can be calibrated by imaging large fluorescent microspheres embedded in a sample.

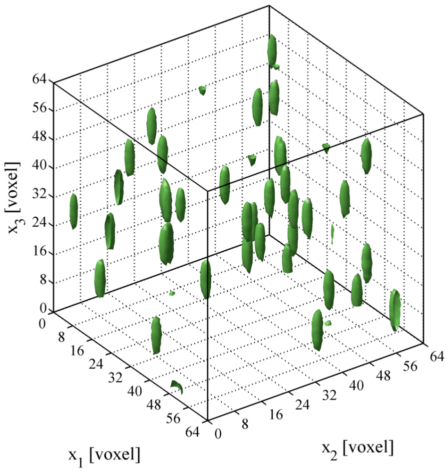

Figure 2.3: Isosurface plot of fluorescent particles as recorded by LSCM (1 voxel = 0.45 μm)

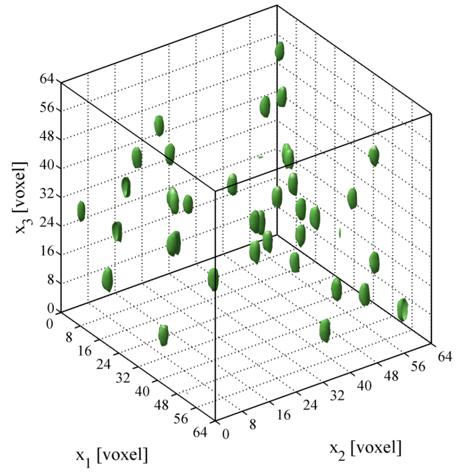

Figure 2.4: Isosurface plot of fluorescent particles after deconvolution of the PSF (1 voxel = 0.45 μm)

2.2 Digital Volume Correlation (DVC)

2.2.1 Principle of DVC

LSCM provides discretized volume images visualizing three-dimensional structural patterns of fluorescent markers in a transparent sample. In this study, the combination of digital volume correlation (DVC) and confocal images is used to achieve three-dimensional full-field deformation measurements as an extension of the vision-based surface deformation measurement techniques, well-known as digital image correlation (DIC) [10]. The basic principle of the DVC is schematically illustrated in Fig. 2.5. Two confocal volume images of an agarose gel with randomly dispersed fluorescent particles are obtained before and after mechanical loading.

Then, the two images are subdivided into a set of subvolumes that are centered on the points of interest. Using each pair of corresponding subvolume images, the respective local displacement vector can be obtained from three-dimensional volume correlation methods. Consider two scalar signals $f(\mathbf{x})$ and $g(\mathbf{x})$ which represent a pair of intensity patterns in a subvolume Ω before and after a continuous mapping, $\hat{\mathbf{y}}(\mathbf{x})\colon \mathbf{x} \to \mathbf{y}$, respectively. Assuming that the signal is locally invariant during the mapping, $f(\mathbf{x}) = g(\mathbf{y}(\mathbf{x}))$, correlation matching by subvolume can be obtained by finding an optimal mapping that maximizes the cross-correlation functional defined as

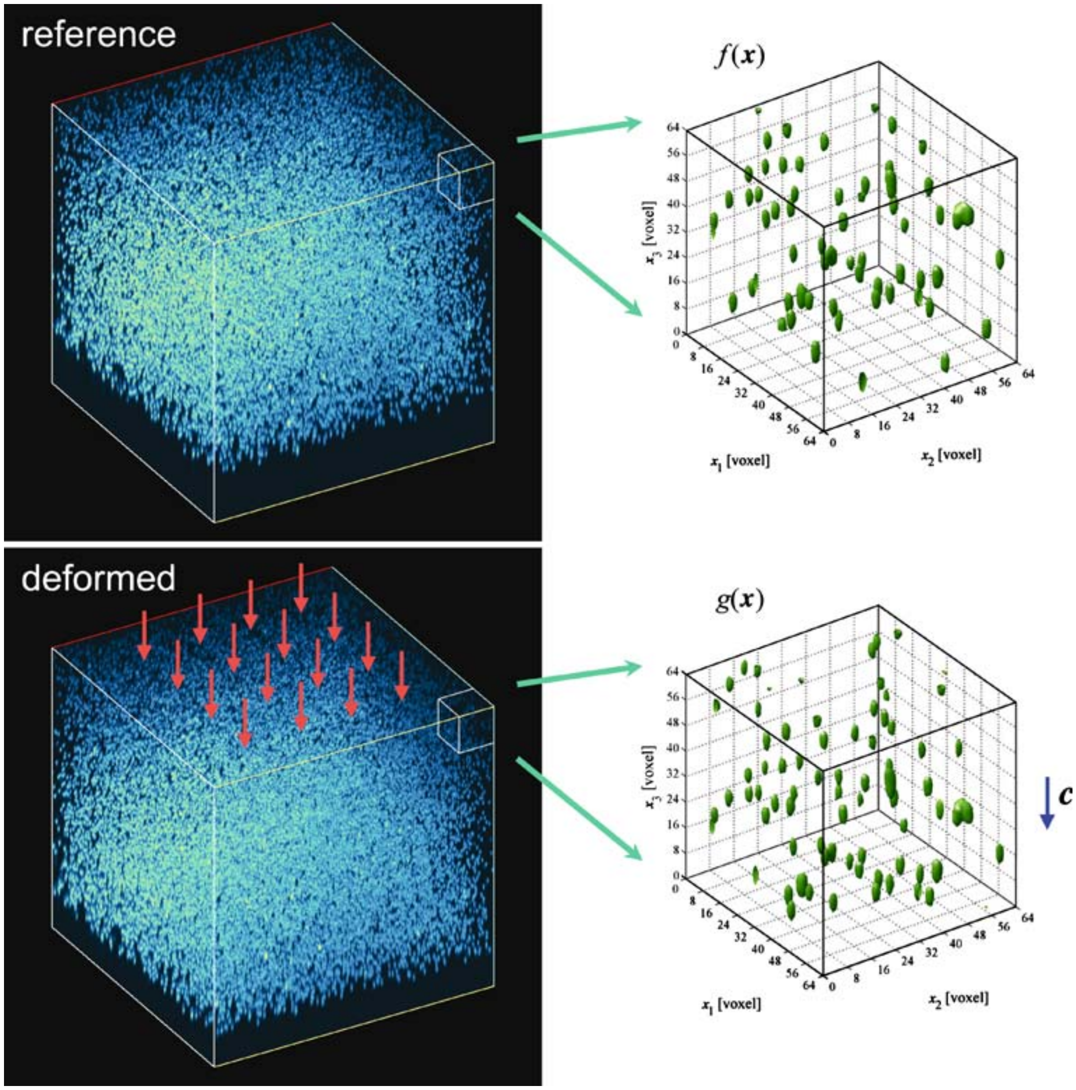

Figure 2.5: Schematic illustration of the principle of digital volume correlation (DVC)

$$m(\hat{\mathbf{y}}) = \int f(\mathbf{x})g(\mathbf{y}(\mathbf{x})d\Omega_x. \tag{2.6}$$

The methodology is illustrated using a translational volume correlation, which is presented below. The continuous mapping is assumed to be a rigid body translation, $\mathbf{y} = \mathbf{x} + \mathbf{c}$, and the cross-correlation function is represented as a function of a displacement vector $\mathbf{c}$ as

$$m(\mathbf{c}) = \int f(\mathbf{x})g(\mathbf{x} + \mathbf{c})d\Omega_x. \tag{2.7}$$

The cross-correlation function can be written using Fourier transforms as

$$m(\mathbf{c}) = \mathscr{F}^{-1}[\mathscr{F}[f(\mathbf{x})]^* \mathscr{F}[g(\mathbf{x})]], \tag{2.8}$$

where the Fourier transform of $f(\mathbf{x})$ is defined as

$$\mathscr{F}[f(\mathbf{x})] = \int f(\mathbf{x}) e^{-ik\cdot\mathbf{x}} d\Omega_x, \tag{2.9}$$

and * denotes the complex conjugate. The discrete cross-correlation function can be computed efficiently by using the fast Fourier transform (FFT) algorithm. Then, the rigid body translation vector $\mathbf{c}$ can be estimated from the location of the cross-correlation peak with respect to the origin. Finding the displacement vector $\mathbf{c}$ from the discrete cross-correlation function is straightforward and provides half-voxel accuracy. Determining the displacement vector $\mathbf{c}$ within subvoxel accuracy generally requires fitting and interpolation of the correlation function near the peak. Various fitting models have been used in the past [9, 48], employing somewhat arbitrary assumptions that the cross-correlation function near the peak can be approximated by a Gaussian or a parabolic function. The subvoxel accuracy of such peak-finding algorithms is determined by the choice of fitting function as well as the size of the fitting window. In this study, a three-dimensional quadratic polynomial fitting is used to fit the correlation function near the peak and hence provides improved subvoxel accuracy over previously used lower order fitting polynomials.

Significant measurement error can be introduced from the decorrelation of the intensity patterns when the rotation or the stretch of the subvolume is large. Thus, applications of such simple correlation algorithms have been limited to small strain and small rotation problems due to the inherent limitation of the rigid-translation assumption. In general, the applicability of such an algorithm is limited up to about 5% of strain or 0.05 radian of rotation [9]. To overcome this limitation and to obtain more accurate displacement measurements, a higher order approximation of the deformation field within each subvolume is required for large deformation measurements in soft materials. In the following section, an extension of the FFT-based DVC to measure large deformation fields is presented.

2.2.2 Stretch Correlation Algorithm

Assuming a general homogeneous deformation of each subvolume, the deformation field can be written as

$$\hat{\mathbf{y}}(\mathbf{x}) = \mathbf{F}\mathbf{x} + \mathbf{c}, \tag{2.10}$$

with a deformation gradient tensor $\mathbf{F} = \mathbf{I} + \nabla\mathbf{u}$ and a displacement vector $\mathbf{u}$. Therefore, any uniform deformation in three-dimensions can be represented with a total of 12 parameters which consist of three displacement components and nine displacement gradient components. Optimal programming in three-dimensions for a total of 12 degrees of freedom (DOF) is computationally expensive in conventional correlation algorithms. Alternatively, the general homogeneous deformation can be represented using a polar decomposition of the deformation gradient tensor as

$$\hat{\mathbf{y}}(\mathbf{x}) = \mathbf{R}\mathbf{U}\mathbf{x} + \mathbf{c}, \tag{2.11}$$

where $\mathbf{R}$ is the orthogonal rotation tensor and $\mathbf{U}$ is the symmetric right-stretch tensor. Then, the general homogeneous deformation in three dimensions is represented with six stretch, three rotation, and three translation components. Depending on the dominant mode of the deformation of interest, the correlation algorithm can be modified to include additional optimization parameters selectively. A digital volume correlation algorithm that includes three rotational degrees of freedom has been presented previously [46]. In this study, assuming small rotations and small shear stretch components, three normal stretch components are included as additional correlation parameters in the FFT-based DVC algorithm, as an extension of the stretch-correlation algorithm developed for large deformation measurements in two dimensions [22]. Neglecting the small rotations, the mapping of a pure homogeneous deformation and a rigid translation is written as

$$\hat{\mathbf{y}}(\mathbf{x}) = \mathbf{U}\mathbf{x} + \mathbf{c}. \tag{2.12}$$

When the loading axes are aligned with the global coordinate axes so that the shear stretch components are small, the invariant condition can be written as

$$f(\mathbf{x}) \approx g(\overline{\mathbf{U}}\mathbf{x} + \mathbf{c}), \tag{2.13}$$

where $\overline{\mathbf{U}}$ denotes the diagonal part of $\mathbf{U}$. Then, the six optimization parameters for the stretch correlation in DVC algorithm are $\{c_1, c_2, c_3, U_{11}, U_{22}, U_{33}\}$. In the case of a pure stretch problem without any translation, a simple coordinate transform into a logarithmic scale converts the stretch correlation problem into a simple translational correlation problem. However, when there is a non-zero translation, the coordinate transform cannot be directly performed in the spatial-domain to achieve the stretch correlation. Therefore, an equivalent invariant condition of Eq. (2.13) in the Fourier domain is considered to implement the stretch correlation in the Fourier domain as

$$||\overline{\mathbf{U}}||\mathscr{F}(\overline{\mathbf{U}}\mathbf{k}) = e^{i\mathbf{k}\cdot\mathbf{c}}\mathscr{G}(\mathbf{k}), \tag{2.14}$$

where, again, $\mathscr{F}(\mathbf{k})$ and $\mathscr{G}(\mathbf{k})$ represent Fourier transforms of $f(\mathbf{x})$ and $g(\mathbf{x})$, respectively. Then by using the Fourier power spectrums only and therefore dropping the phase term, a translation-invariant stretch-correlation problem can be achieved in the Fourier domain. A stretch cross-correlation function to be maximized for determining the three axial stretch components neglecting the determinant of the Jacobian is shown as

$$m(\overline{\mathbf{U}}) = \int |\mathscr{F}(\overline{\mathbf{U}}\mathbf{k})||\mathscr{G}(\mathbf{k})| d\Omega_x. \tag{2.15}$$

The stretch correlation problem in the Fourier domain can be transformed into a translational correlation problem in a log-frequency domain as

$$\widetilde{m}(\boldsymbol{\eta}) = \int |\widetilde{\mathscr{F}}(\boldsymbol{\xi} + \boldsymbol{\eta})||\widetilde{\mathscr{G}}(\boldsymbol{\xi}) d\Omega_\xi, \tag{2.16}$$

where $\boldsymbol{\xi} = log_b\mathbf{k}$, $\boldsymbol{\eta} = log_b\overline{\mathbf{U}}$, and b is an arbitrarily chosen logarithmic base. The translational correlation problem in the log-frequency domain can be easily solved using Eq. 2.8. Finally, the three axial stretch components can be obtained from the optimal vector $\boldsymbol{\eta}$ in the log-frequency domain as

$$U_{11} = b^{\eta_1}, \quad U_{22} = b^{\eta_2} \quad and \quad U_{33} = b^{\eta_3}. \tag{2.17}$$

The accuracy of the obtained stretch components depends strongly on the spectral content of the original signals. If the signals are already band-limited, special considerations, such as normalizing the power spectrums and employing the Hanning window, must be included to achieve robust stretch correlations. Also, in the numerical implementation of the stretch correlation algorithm, incorporating zero-padding of the signals before Fourier transforms can improve the overall accuracy of the stretch correlation algorithm by providing ideal interpolations of the Fourier transforms at a cost of increased computational load.

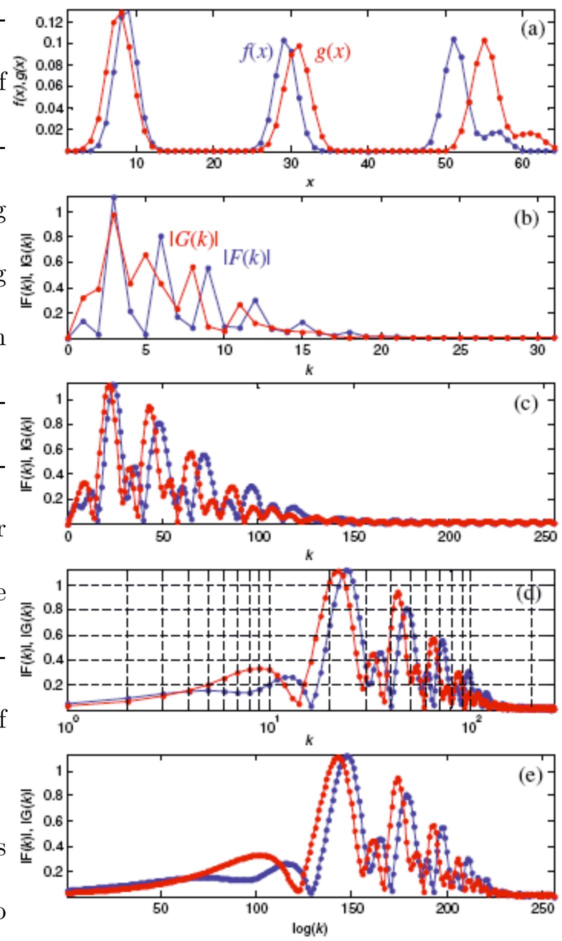

Figure 2.6: Illustration of the stretch-correlation procedures using a one-dimensional (1D) example

In Fig. 2.6, the stretch-correlation procedures are illustrated for a one-dimensional example. Two reference and deformed signals representing 10% of uniform strain are shown in Fig. 2.6 (a). The Fourier power spectra of the two signals are shown in Fig. 2.6 (b). Note that only half of the full frequency range is shown due to the inherent Fourier symmetry. In Fig. 2.6 (c), the equivalent Fourier power spectra are shown after applying zero-padding (interpolation) to the power spectra in Fig. 2.6 (b). Figure 2.6 (d) shows the Fourier power spectra along the logarithmic axis. After interpolating the power spectra using a uniform interval in the log-frequency domain as shown in Fig. 2.6 (e), the translational correlation as presented in Eq. 2.16 can be applied to find the one-dimensional stretch value. Extension of the one-dimensional stretch-correlation into two dimensions or three dimensions is straightforward as long as the rotations and shear stretches are small.

In the implementation of three-dimensional stretch correlation, two-dimensional projections of the three-dimensional subvolume images were used to circumvent the geometrically increased computational load after the zero-padding, as shown in Fig. 2.7. Essentially, the stretch correlations using the large zero-padding were conducted in a reduced dimension for computational efficiency. Three separate two-dimensional projections were made so that three sets of two stretch components could be obtained. From the six stretch values, three stretch components (U_{11}, U_{22}, U_{33}) were obtained by computing the average of the two corresponding stretch components. Once the three axial stretch components are found, the translation vector $\mathbf{c}$ can be determined more accurately by conducting the stretch-compensated translational correlation using

$$m(\mathbf{c}) = \int \widetilde{f}(\boldsymbol{x}')g(\boldsymbol{x}' + \mathbf{c})d\Omega_x, \tag{2.18}$$

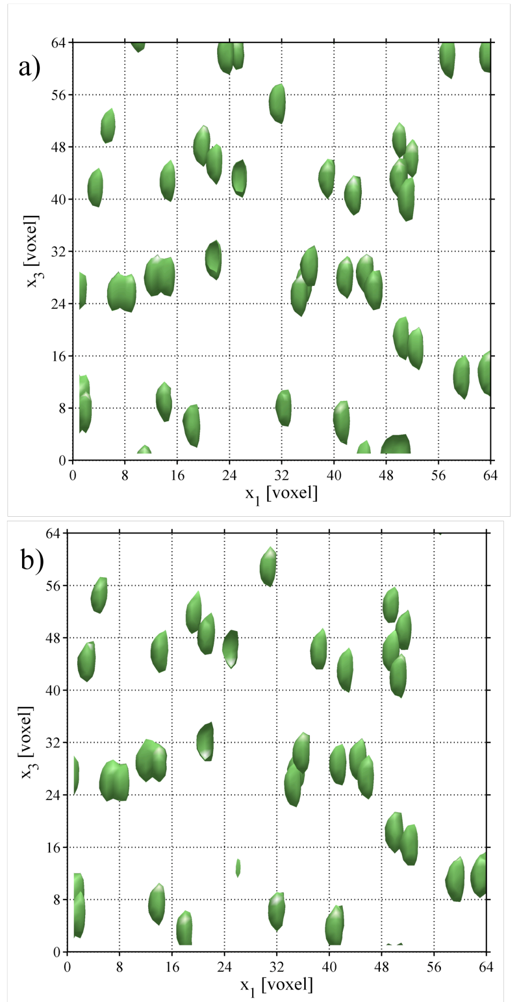

Figure 2.7: Two-dimensional projection of confocal subvolume images (a) before and (b) after uniaxial compression of 10% in x_3-direction

where $f(\mathbf{x}) = \widetilde{f}(\overline{\mathbf{U}}\mathbf{x})$ and $\boldsymbol{x}' = \overline{\mathbf{U}}\mathbf{x}$. The stretch-compensated translational correlation requires the initial subvolume image $f(\mathbf{x})$ to be stretched to $\widetilde{f}(\boldsymbol{x}')$ using the three stretch values obtained earlier. Therefore, the process involves sub-voxel interpolations of the initial subvolume image. Because the stretch part of the deformation is compensated, a more accurate translation vector **c** can be obtained. The stretch correlation and the translational correlation were conducted iteratively to achieve converged results. For all experiments executing the stretch and translational correlation twice yielded sufficient convergence based on a mean difference criterion, where the mean and standard deviation of the difference of the before and after displacement matrices were compared (this is similar to the least-square error estimate). Such an iteration process is equivalent to the iterative optimization of a correlation coefficient in conventional image correlation scheme conducted in the two-dimensional spatial domain.

Finally, the displacement gradients were computed by using a three-dimensional least-square fitting of each displacement component in a 3 x 3 x 3 grid of neighboring data points. Although a more sophisticated smoothing or filtering algorithm can be employed before or during the gradient calculation to obtain smoother strain fields, no such algorithm was used in this study to assess the performance and robustness of the proposed DVC algorithm. Once the displacement gradient fields are determined, either infinitesimal or finite strain values can be computed from the displacement gradient fields.

2.3 Experimental Procedures

Agarose test specimens were prepared from a 1% weight-in-volume (w/v) solution of agarose (J.T. Baker, NJ) in standard 0.5X TBE buffer (Tris/Borate/EDTA, pH 8.0). The agarose solution was heated until molten, and carboxylate-modified red fluorescent (580/605) polystyrene microspheres (Invitrogen, CA) of 1 μm diameter were injected into the liquid agarose. The nominal volume fraction of fluorescent markers in the gel was 0.3%. The mixture was cast into a pre-chilled Teflon mold mounted onto a glass plate. Samples were left at room temperature for 5 minutes to solidify.

This protocol yielded circular agarose specimens with typical dimensions of 6.4 mm diameter and 1.4 mm height. The addition of the fluorescent microspheres had negligible effect on both the local and global mechanical response of the agarose gel. For spherical inclusion measurements describing a hard inclusion surrounded by a soft matrix, spherical polymethylmethacrylate (PMMA) beads

(Sigma-Aldrich, MO) of 100 μm diameter were added to the mixture before casting. For spherical inclusion measurements describing a soft inclusion of a hard matrix, a burst of air was injected into the molten agarose gel to allow the formation of voids inside the material. The air inclusions (bubbles) were consequently imaged and a particular isolated bubble (only bubble within entire field of view) with a diameter of 200 μm was chosen.

To apply uniaxial compressive loading to the sample while imaging, a miniature loading-fixture was built and mounted directly on the microscope stage of an inverted optical microscope as shown in Fig. 2.8. The sample was kept immersed in the buffer solution to prevent swelling or shrinking during the test. The compressive loading was achieved by translating a micrometer head with a resolution of 1 μm. For all experiments the imposed strain increments were controlled by the micrometer (Mc Master-Carr, Los Angeles, CA) and were calculated using the dimension of the specimen and the imposed loading (displacement) step. The resulting applied force was measured using a 10-gram load cell (A.L. Design, NY). Nominal stress-strain curves were compiled using this setup for each test. The LSCM used in this study was a confocal system (Nikon C-1) combined with an inverted optical microscope (Nikon TE-2000-U). A 40x CFI planar fluor air objective with a numerical aperture of 0.6 was used in all experiments. All DVC computations were performed using Matlab (Mathworks, Natick, MA), and executed on an Intel based Pentium Xeon with 4 core processors. The typical computation time for 512 x 512 x 512 voxel image with a spatial resolution of 8 voxels is ~ 4.3 hours/image.

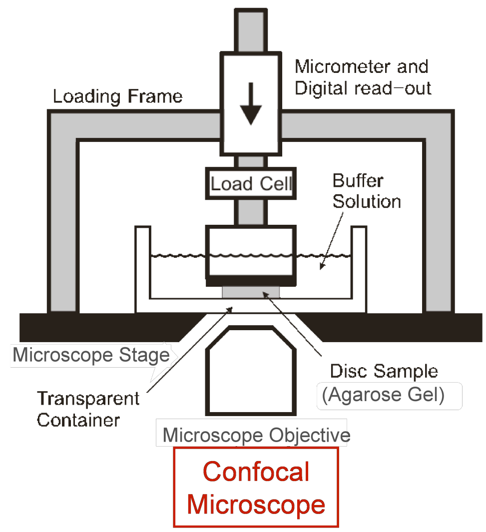

Figure 2.8: Loading fixture for uniaxial compression of soft materials mounted onto a laser scanning confocal microscope

	Stationary	Translation
u_1 [voxel]	0.0605	0.1392
u_2 [voxel]	0.0541	0.1238
u_3 [voxel]	0.2106	0.6491
ϵ_{11} (%)	6.39 x 10^{-3}	4.18 x 10^{-2}
ϵ_{22} (%)	9.80 x 10^{-3}	4.96 x 10^{-2}
ϵ_{33} (%)	0.260	0.718

Table 2.1: Standard deviation values for measured displacement and strain fields in the undeformed condition

2.4 Uniaxial Compression Results

To verify the measurement precision of the DVC algorithm using confocal volume images, two tests were conducted under zero-strain condition. In the first test, two confocal volume images were repeatedly acquired from a stationary sample under zero load. The scanning resolution was 512 x 512 x 512 voxels, and the scan spacing was 0.45 µm in all three directions. This resulted in a field of view of 230 x 230 x 230 μm^3. In the second test, confocal images were acquired before and after translating the unloaded sample using the x_3-directional scanning stage of the confocal microscope. The two pairs of the confocal images were analyzed by using the DVC algorithm with a subvolume size of 64 x 64 x 64 voxels. Displacements were measured at 15 x 15 x 15 points (total 3375 points) in a uniform grid of 32 voxels spacing. Displacement gradients were then calculated by using the displacement data at 3 x 3 x 3 neighboring grid points following linear least-square fitting of the displacement components. Although the quadratic (Lagrangian) or the logarithmic (true) strain measure can be used for large deformation analysis, the linear (engineering) strain measure was used to represent the deformations in this study. As a quantitative measure of the uncertainties in the DVC results, standard deviation values of three displacement components and three normal strain components were computed and are summarized in Table 2.1.

The absolute values of the uncertainties in the displacements and the strains are comparable to previously reported results [4, 39]. These measurement uncertainties are likely due to the noise in the confocal images caused by the photomultiplier tube detector noise as well as the positional uncertainty of the laser scanning system. It is also noted that the axial uncertainties of the displacement and strain components in the x_3-direction (axial) are approximately three to five times larger than the corresponding lateral uncertainties in the x_1- and x_2-directions (in-plane). This result shows that the axially elongated three-dimensional point spread function causes a significantly degraded measurement precision in the x_3-direction. These tests under zero-strain condition provide a simple way to assess baseline uncertainties of the measurements using the DVC algorithm.

In order to verify the three-dimensional deformation measurement capability of the DVC using the LSCM, the agarose gel sample was compressed uniaxially with nominal strain increments of 2-3%. The total imposed nominal strain was approximately 10%. The obtained confocal images were analyzed using the DVC algorithm with a subvolume size of 64 x 64 x 64 voxels. Figure 2.10 shows a vector plot of the measured displacement field and Fig. 2.9 shows a three-dimensional contour plot of the vertical displacement components.

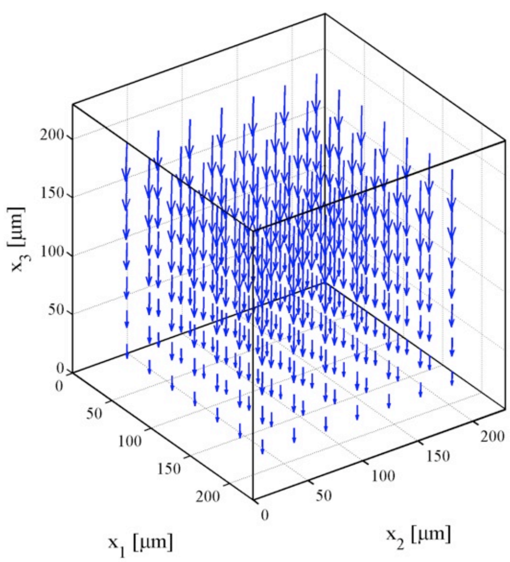

Figure 2.9: Experimentally determined three-dimensional displacement vector field under uniaxial compression

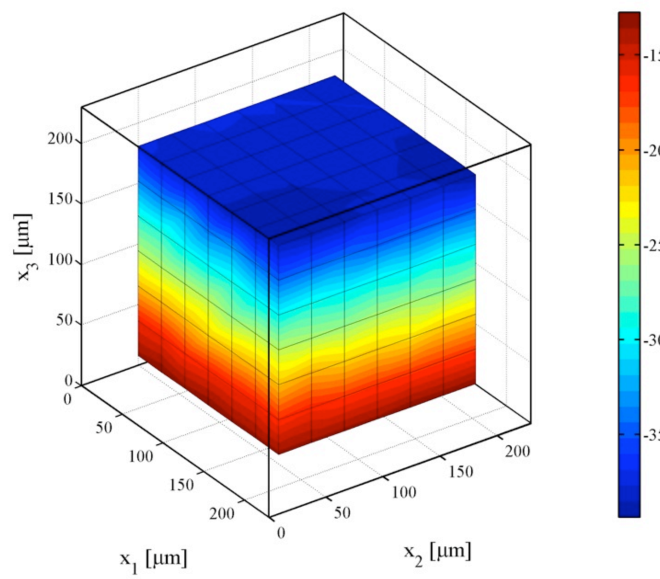

Figure 2.10: Experimentally determined vertical displacement field u_3 under uniaxial compression

In order to assess the performance of the DVC algorithm with the stretch-correlation for large deformation measurements, accuracy and precision must be established systematically. The accuracy and the precision of a measurement technique are usually achieved by repeatedly measuring some traceable reference standard. Then, the accuracy and precision are typically quantified as

	No stretch-correlation		Stretch-correlation	
	Mean	Std. Deviation	Mean	Std. Deviation
ϵ_{11} (%)	0.8 x 10^{-2}	7.1 x 10^{-2}	-3.6 x 10^{-2}	7.4 x 10^{-2}
ϵ_{22} (%)	1.1 x 10^{-2}	6.8 x 10^{-2}	7.8 x 10^{-2}	7.1 x 10^{-2}
ϵ_{33} (%)	-9.25	0.866	-9.34	0.392

Table 2.2: Mean and standard deviation values for measured strain fields under uniaxial compression

the difference between the mean of the measured values and the true value, and by the standard deviation of the measured values, respectively.

Mean and standard deviation values of the measured strain fields are presented in Table 2.2 to assess the effectiveness of the stretch-correlation algorithm. The mean values of the lateral strain components ϵ_{11} and ϵ_{22} are close to zero and smaller than their corresponding standard deviation values, i.e., the measurement precision, and are therefore negligible. The standard deviations of the no-stretch-correlated and stretch-correlated lateral strain components are similar, illustrating that the stretch-correlation does not improve the precision of the strain measurements for small strains. Comparing the no-stretch and stretch-corrected axial strain component ϵ_{33}, the difference of 0.09% between the two mean values is smaller than their corresponding standard deviations, which shows that the stretch correlation does not improve the accuracy of the average strain measurement. However, the standard deviation in the stretch-correlation case is less than half of that in the no-stretch-correlation case. This proves that the stretch-correlation greatly improves the precision of the large deformation measurement. Although precise measurements do not necessarily mean accurate measurements, it is often not possible to reliably achieve high accuracy in individual measurements without precision. This point is particularly important in the full-field measurement of non-uniform deformation fields.

Since it is not possible to know the true value of the compressive strain up to the level of accuracy and precision of the measurement technique under investigation, the absolute accuracy of the proposed DVC method cannot be assessed with the nominal strain value from the global measurement. However, it is clear that the overall measurement accuracy can be improved by providing better precision, since precision is a limit of accuracy. The results from the uniaxial compression test show that the proposed stretch-correlation algorithm in conjunction with the deconvolution algorithm improved the overall accuracy of large deformation measurement with better precision.

The average axial compressive strain was 9.3%, whereas the average lateral strain values were negligible. This result showed that the lateral expansion due to the Poisson effect was effectively constrained due to the disc-shaped geometry of the sample. To determine the material properties of the agarose sample correctly the uniaxial test results need to be interpreted as a constrained compression ($\epsilon_{11} = \epsilon_{22} = 0$) of a soft layer. The axial stress-strain ratio for constrained compression is defined as a constrained modulus ($\overline{E}$) and related to elastic properties as

$$\overline{E} = \frac{\sigma_{33}}{\epsilon_{33}} = \frac{(1-\nu)E}{(1+\nu)(1-2\nu)}, \tag{2.19}$$

where E and ν denote the Young's modulus and the Poisson's ratio, respectively.

2.5 Spherical Inclusion Results

In order to demonstrate the capability of the measurement technique using the DVC and the LSCM, non-uniform three-dimensional deformation fields near a hard and a soft (void) spherical inclusion were measured under far-field uniaxial compressive loading. Confocal images near a 100 µm-diameter PMMA bead and a 200 µm air bubble embedded within the agarose gel sample were recorded during incremental compressive loading. The experimental setup is shown in Fig. 2.11 schematically. The nominal strain increment was approximately 3%. The scanning resolution was 512 x 512 x 512 voxels, and the scan spacing was 0.45 µm

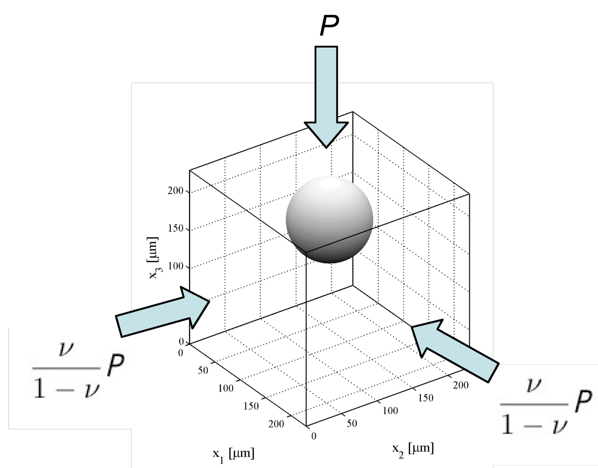

Figure 2.11: Schematic of a spherical inclusion with a sliding interface under confined uniaxial compression

in all three directions. The experimentally determined displacement fields were qualitatively and quantitatively compared to the analytical solution given by Ghahremani [18] and is presented in the next section. The solution by Ghahremani describes a spherical "sliding" inclusion, where the "sliding" is defined by vanishing tractions along the inclusion-matrix interface and continuity in the displacements normal to the inclusion-matrix interface.

2.5.1 Analytical Solution of a Sliding Spherical Inclusion

This section presents the analytical solution of a sliding spherical inclusion in a linearly elastic matrix under applied far field uniaxial compressive loading as formulated by Ghahremani [18] . Most analytical elasticity solutions of the inclusion problem assume the continuity of displacement at the interface. Considering the high water content in the agarose gel and the large deformations in the sample, the perfect bonding condition is inadequate to accurately represent the present experiment. Using the solution of the sliding inclusion problem under uniaxial loading, and considering that only the deformations inside the agarose gel and not the inclusion itself are measured, the elasticity solution of the matrix displacements beginning with the far field solution due to an applied uniform compressive loading stress P is

$$u_\infty = \frac{P}{2G_m(1+\nu_m)}(\nu x_1\mathbf{i} + \nu x_2\mathbf{j} - x_3\mathbf{k}), \tag{2.20}$$

where G_m and ν_m denote the shear modulus and Poisson's ratio of the matrix, respectively, and **i**, **j**, **k** are the Cartesian unit vectors. The radial displacements due to the inclusions are

$$u_r(r,\theta) = -\frac{A}{r^2} + [\frac{B(5-4\nu_m)}{r^2} - \frac{3C}{2r^4}](3cos^2\theta - 1), \tag{2.21}$$

with $r = \sqrt{x_1^2 + x_2^2 + x_3^2}$, and $\theta = tan^{-1}(x_3/\sqrt{x_1^2 + x_2^2})$, and constants A, B, and C as described later. The tangential displacements due to the inclusion are

$$u_\theta(r,\theta) = -[\frac{B(1-2\nu_m)}{r^2} + \frac{C}{2r^4}](sin2\theta). \tag{2.22}$$

The constants A, B, and C are defined as

$$A = \frac{Pr_0^3}{12G_m} - \frac{Dr_0^3(1+\nu_i)G_i}{G_m}, \tag{2.23}$$

$$B = -\frac{5P}{12G_m} \cdot \frac{r_0^3}{7-5\nu_m} + \frac{G_i}{G_m} \cdot \frac{7+5\nu_i}{7-5\nu_m} Fr_0^5, \tag{2.24}$$

$$C = -\frac{P}{2G_m} \cdot \frac{r_0^5}{7-5\nu_m} + \frac{G_i}{2G_m} - \frac{1+\nu_m}{7-5\nu_m}(7+5\nu_i)Fr_0^7, \tag{2.25}$$

where G_i and ν_i denote the shear modulus and Poisson's ratio of the inclusion, respectively, r_0 is the inclusion diameter, and the constants D and F are given by

$$D = \frac{P(1-\nu_m)}{4(1+\nu_m)[(2G_m+G_i)+\nu_i(G_i-4G_m)]}, \tag{2.26}$$

$$F = \frac{-10P(1-\nu_m)}{r_0^2[4G_m(7-5\nu_m)(4\nu_i-7)-G_i(17-19\nu_m)(7+5\nu_i)]}. \tag{2.27}$$

The final form of the analytical solution of the sliding inclusion under the laterally-constrained uniaxial compressive loading is constructed by the superposition of three mutually-orthogonal uniaxial compression solutions using Eqs. (2.20-2.27) as illustrated in Fig. 2.11.

2.5.2 PMMA Bead and Air Bubble Inclusion Results

This section presents the experimentally determined full-field three-dimensional displacements near a hard (PMMA) and soft (air bubble) inclusion. Confocal images of each embedded inclusion were recorded during successive compressive loading increments. The nominal strain increment was approximately 3%. The scanning resolution was 512 x 512 x 512 voxels as before, and the scan spacing was 0.45 μm in all three directions. A representative confocal scanning volume near the inclusion is illustrated schematically in Fig. 2.11. Figures 2.12 and 2.13 show a vertical slice of the confocal image along the meridian plane of the PMMA bead and the air bubble at the undeformed configuration, respectively. The superimposed uniform grid with spacing increments of 16 voxels represents the locations where displacements measurements were conducted. The confocal images were analyzed by using the proposed DVC algorithm with a subvolume size of 64 x 64 x 64 voxels. The spatial resolution of the DVC technique can be adjusted and increased to a maximum resolution of 1 voxel. However, due to the increased computational load with increased resolution, the typical spatial resolution for calculating the displacement is 8 voxels, or 3.6 μm.

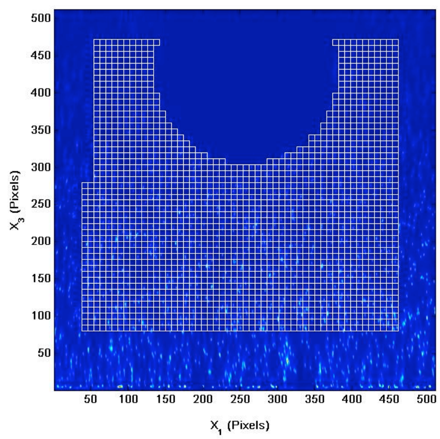

Figure 2.12: Confocal slice along the meridian plane of an embedded 100 μm PMMA bead within an agarose sample

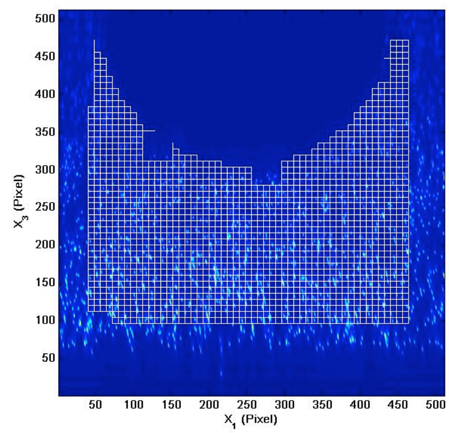

Figure 2.13: Confocal slice along the meridian plane of an embedded 200 μm air bubble within an agarose sample

Initially, the displacement fields are calculated using the translational DVC algorithm, the output of which is then used as an initial guess in calculating the displacement fields using the stretch-correlation algorithm. Figures 2.14 and 2.15 show a representative cross-sectional three-dimensional contour plot of the u_3 displacement fields near the PMMA bead and air bubble inclusion. Figures 2.16 and 2.17 show the results of the DVC stretch-correlation algorithm for the same experimental data on a smaller data domain (around the center plane of each inclusion). Since the stretch-correlation algorithm is computationally more expensive than the regular translational DVC algorithm, only a particular region of interest, which here is a volumetric region around the center plane of each inclusion, is selected. In order to compare the experimental data with the analytical elasticity solution presented in the previous section, the data set is refined further by selecting and executing the DVC stretch-correlation on the meridian plane of each inclusion. The voxel spacing or spatial resolution of the DVC measured displacement field is further increased to a grid spacing of 4 voxels. Generally such an increase in resolution is only performed on thin volumes consisting of less than 10 slices to be computationally efficient.

The contour maps in Figs. 2.18 and 2.19 represent constant contours of the vertical (u_3) displacement components on the meridian plane of the PMMA and air bubble inclusion, respectively. The local distortion of the displacement contours near the PMMA bead and the air bubble indicate that the proposed DVC algorithm effectively captures non-uniform deformation fields near both spherical inclusions. It should be noted that the magnitude of the u_3 displacements as indicated in pixels by the color bar in both Figs. are different. This difference is due to rigid body translation during the experiments that is also captured by the DVC algorithm. This rigid body motion arises since the imaging reference frame is stationary and the inclusion location within the agarose gel is different for the two inclusions. Hence, the amount of recorded rigid body translation will be different. The rigid body translation is accounted for in the analytical model through the simple addition of a displacement constant. The experimentally measured displacement fields in Figs. 2.18 and 2.19 were compared to the analytical solution of the equivalent linear-elasticity problem as described in detail in the previous section.

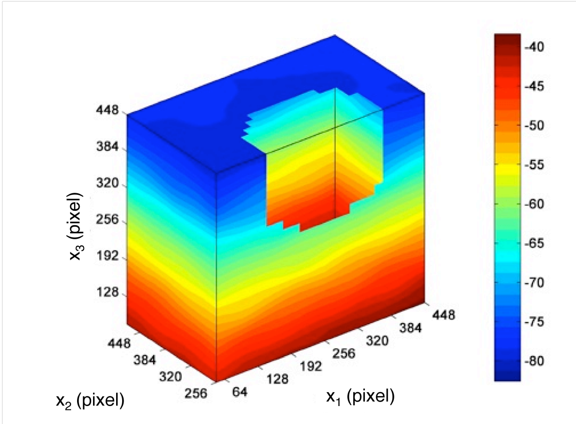

Figure 2.14: Cross-section of the experimentally determined vertical displacement field u_3 near PMMA bead inclusion under uniaxial compression. Contour values are in pixels (1 pixel = 0.45 μm).

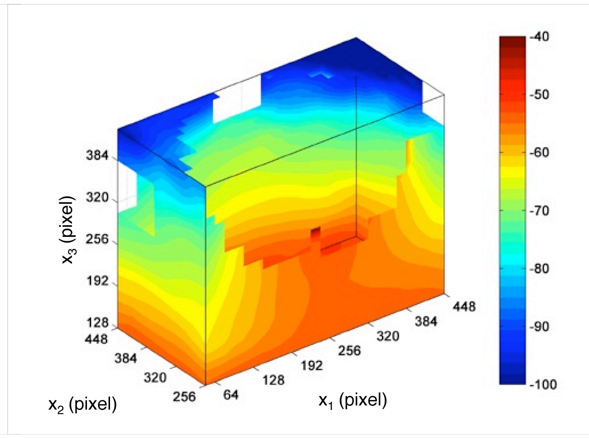

Figure 2.15: Cross-section of the experimentally determined vertical displacement field u_3 near air bubble inclusion under uniaxial compression. Contour values are in pixels (1 pixel = 0.45 μm).

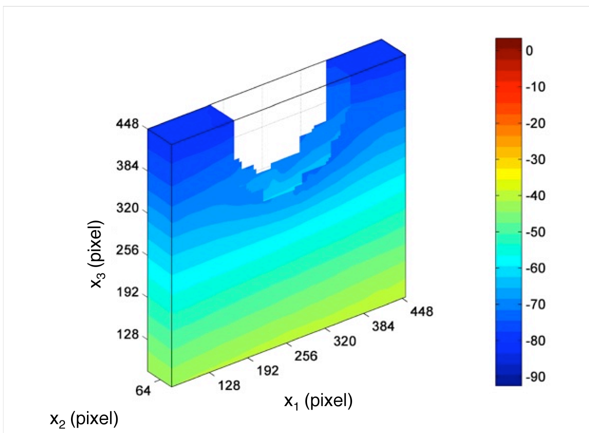

Figure 2.16: Cross-section of the stretch-corrected measured vertical displacement field u_3 near the PMMA bead inclusion under uniaxial compression. Contour values are in pixels (1 pixel = 0.45 μm).

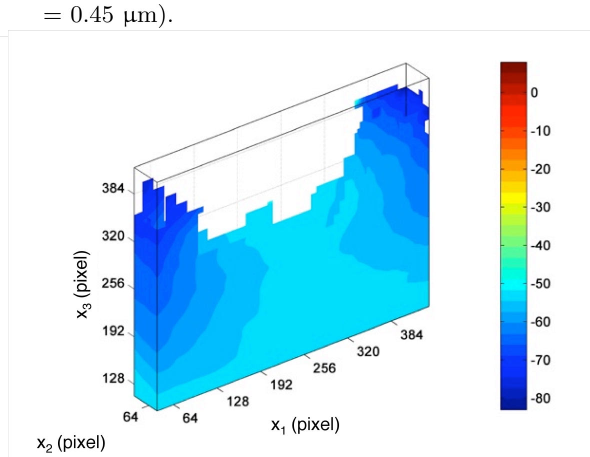

Figure 2.17: Cross-section of the stretch-corrected measured vertical displacement field u_3 near the air bubble inclusion under uniaxial compression. Contour values are in pixels (1 pixel = 0.45 μm).

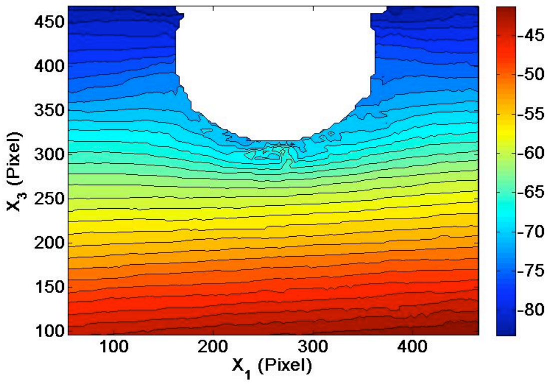

Figure 2.18: Experimentally determined vertical displacement field u_3 near PMMA bead inclusion under uniaxial compression. Contour values are in pixels (1 pixel = 0.45 μm).

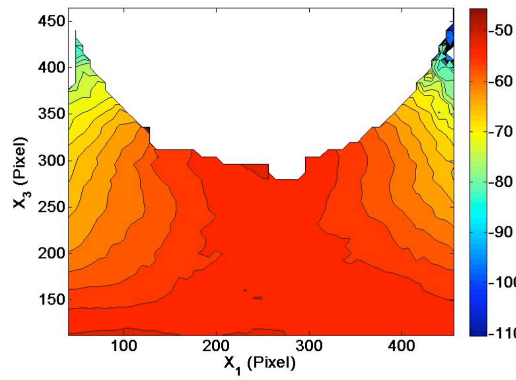

Figure 2.19: Experimentally determined vertical displacement field u_3 near air bubble inclusion under uniaxial compression. Contour values are in pixels (1 pixel = 0.45 μm).

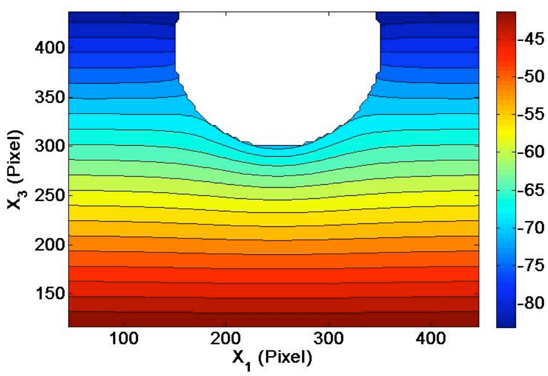

Figure 2.20: Analytical vertical displacement field u_3 near a rigid bead inclusion with a sliding interface under uniaxial constrained compression. Contour values are in pixels (1 pixel = 0.45 μm).

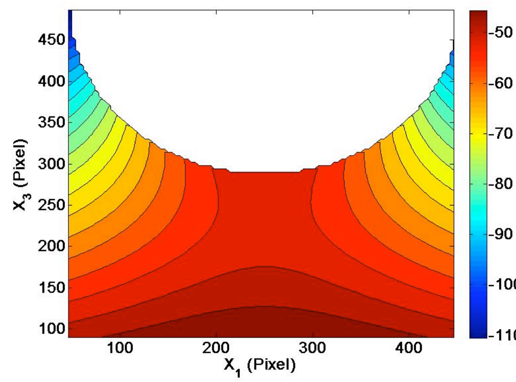

Figure 2.21: Analytical vertical displacement field u_3 near a soft inclusion with a sliding interface under uniaxial constrained compression. Contour values are in pixels (1 pixel = 0.45 μm).

The contour maps in Fig. 2.20 and Fig. 2.21 show the horizontal and the vertical displacement fields of the constructed analytical solution. Qualitative comparisons of the contour maps in Fig. 2.18 and Fig. 2.20, and Fig. 2.19 and Fig. 2.21 indicate that the proposed DVC algorithm is well-suited for the full-field measurements of non-uniform deformation fields in three dimensions. Once the full field displacements are obtained, the strain tensor is calculated by using a displacement-gradient technique [26]. In brief, the local displacement field around each grid point is approximated by

$$\hat{\mathbf{u}}(x_1, x_2, x_3) = ax_1 + bx_2 + cx_3 + d, \tag{2.28}$$

where a,b,c, and d are constants to be determined by minimizing the following vector $\mathbf{S}$ in the least-square sense using the measured displacement vector $\mathbf{u}$

$$\mathbf{S} = \sum_{i=1}^{N}\sum_{j=1}^{M}\sum_{k=1}^{P}(\hat{u}_{ijk} - u_{ijk})^2. \tag{2.29}$$

Point-wise least-square minimization of Eqs. 2.28 and 2.29 using a 3 x 3 x 3 voxel stencil or kernel, yields the constants a,b,c and d from which the full-field strain tensor is constructed. A more detailed description of the displacement-gradient technique can be found in [26]. Figures 2.22 and 2.23 show a contour plot of ϵ_{33} from the experimentally obtained displacement fields around the PMMA and air bubble inclusions, respectively.

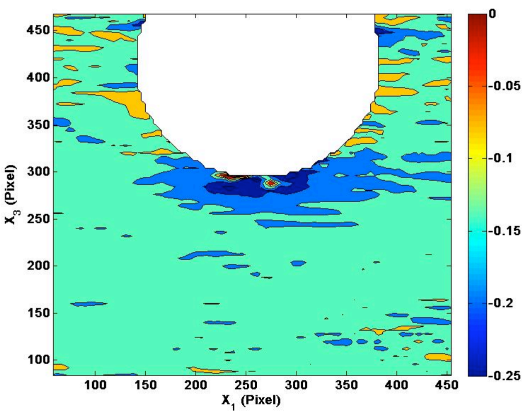

Figure 2.22: Experimentally determined vertical strain field ϵ_{33} near a PMMA bead inclusion under uniaxial compression

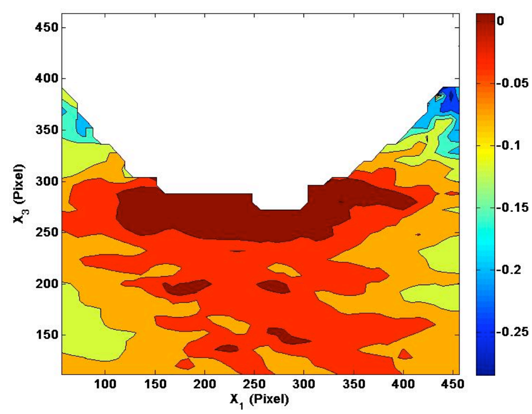

Figure 2.23: Experimentally determined vertical strain field ϵ_{33} near an air bubble inclusion under uniaxial compression

At the bottom of the inclusion in Fig. 2.22, a region of high strain concentration of up to 25% strain, or 2.5 times of the far field applied strain is shown. Figure 2.23 displays a similar picture in case of the strain profile near the air bubble, where ϵ_{33} is approximately zero directly beneath the bubble. Following the time-lapse series of the air bubble compression measurements (not shown here), the air bubble collapses under the applied far field strain with no noticeable deformation occurring in the agarose gel underneath the bubble. Figure 2.24 displays the line-profile of the ϵ_{33} strain component along the central axis in the x_3-direction from the PMMA bead inclusion contour plot (Fig. 2.22). Also shown in Fig. 2.24 is the analytical description of ϵ_{33} along the meridian plane of a hard inclusion as described by Ghahremani [18]. The local compressive strain reaches the far-field applied strain level at approximately one diameter length away from the center of the bead. The high strain gradient will decrease the accuracy of the stretch-correlation by violating the assumption of uniform stretch deformation. In such cases, iterative applications of the DVC using a smaller subvolume will increase the accuracy of the measurements since each subvolume will be subjected to a more uniform stretch.

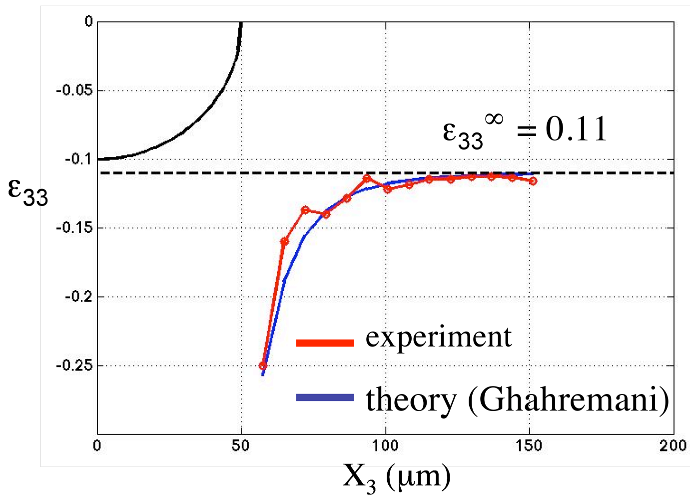

Figure 2.24: Plot of the experimentally determined strain field ϵ_{33} as a function of outward distance ($x_3 = 0$ denotes the center of the inclusion) in the meridian plane of the spherical PMMA inclusion under uniaxial compression

2.6 Summary of LSCM and DVC Development

A novel experimental technique for measuring three-dimensional large deformation fields in soft materials has been developed [17]. The technique utilizes the three-dimensional measurement capability of the DVC algorithm in conjunction with the three-dimensional imaging capability of laser scanning confocal microscopy. Introduction of the stretch-correlation algorithm and the deconvolution algorithm greatly improved the strain measurement accuracy by providing better precision especially under large deformation. Also, the large deformation measurement capability of the proposed DVC algorithm was successfully demonstrated by measuring a uniform deformation field for the case of simple uniaxial compression and a non-uniform deformation field surrounding both a hard and soft (void) spherical inclusion. This new technique should prove particularly useful in situations where local three-dimensional strain non-uniformities need to be measured with high resolution. An application of this technique in characterizing the three-dimensional time-dependent cell interactions with its surrounding extracellular matrix are documented in the following chapters. While it is anticipated that this technique will lead to valuable insights into the role of mechanical forces on biological processes and mechanical characterization of biological materials in three dimensions, the application of the DVC itself is not limited to usage with LSCM. Since DVC is a post-processing technique, it renders itself as a quantitative full-field displacement measurement technique that can be combined with many methods in experimental mechanics including computer tomography (CT) scanning, magnetic resonance imaging (MRI), and many others.